Thin Solid Films 705 (2020) 137978

Contents lists available at ScienceDirect

Thin Solid Films

journal homepage: www.elsevier.com/locate/tsf

# $p^+$ polycrystalline silicon growth via hot wire chemical vapour deposition for silicon solar cells

Edris Khorani[a,*], Tudor E. Scheul[a], Antulio Tarazona[b], John Nutter[c], Tasmiat Rahman[a], Stuart A. Boden[a]

[a] School of Electronics and Computer Science, University of Southampton, SO17 1BJ, United Kingdom
[b] Optoelectronics Research Centre, University of Southampton, Southampton, SO17 1BJ, United Kingdom
[c] Henry Royce Institute, University of Sheffield, Sheffield, S10 2TN, United Kingdom

ARTICLE INFO

*Keywords:*
Hot wire chemical vapour deposition
Silicon solar cells
Emitter
Crystallisation
Transmission electron microscopy
Selective area electron diffraction

ABSTRACT

Hot wire chemical vapour deposition (HWCVD) is explored as a way of growing boron-doped silicon for photovoltaic devices. Deposition temperatures are measured using a custom-built monitoring system for two different filament configurations within the HWCVD tool. A refined fabrication process is presented, using an altered filament arrangement, that currently provides a maximum deposition temperature of 535 °C, for growing boron-doped silicon films via HWCVD, with the inclusion of a short post-deposition anneal at 800 °C for 2 min. Transmission electron microscopy reveals improvements in interfacial quality, as well as larger grains, present after post-annealing treatments. In addition, re-crystallisation of as-deposited amorphous Si films under a short anneal is confirmed using Raman spectroscopy. The enhancements in morphology translate to a boost in current rectification based on dark current-voltage measurements. This is further supported by secondary-ion mass spectrometry analysis, presenting $p^+$ properties with uniform doping in the $10^{21}$ $cm^{-3}$ region.

## 1. Introduction

Crystalline silicon solar cell technology encompasses over 90% of the commercial photovoltaic (PV) market and is expected to maintain this over the next decade [1]. Amongst the various architectures, the all back-contact design has gained increasing attention in the PV community as it allows for higher optical absorption due to no shading losses from front surface contacts. Conventionally, thermal diffusion is used for doping of the emitter and back surface field regions [2,3]. Despite this architecture consistently achieving high efficiencies beyond 20% across literature, the production cost and complexity of interdigitated diffused junctions remain an issue [2–5]. We study silicon growth using hot wire chemical vapour deposition (HWCVD), with in-situ doping, as a low-cost alternative to forming these diffused structures.

HWCVD has developed to become a mature form of chemical vapour deposition (CVD) when compared to other CVD tools [6]. Multiple groups have managed to produce amorphous, microcrystalline and polycrystalline silicon thin films using this tool, with doping both p-type and n-type proving feasible [7,8]. Selective area epitaxial film growth on silicon wafers has also shown viability [9,10]. HWCVD is attracting attention for making higher quality interfaces by avoiding plasma damage of the substrate. Furthermore, the efficiency of gas use during growth is much higher than other CVD techniques, being up to ten times higher than that of plasma-enhanced CVD (PECVD) [11]. The relatively fast deposition rates and single-sided deposition method, as well as the large-area deposition coverage of the tool, makes scaling HWCVD towards commercial applications favourable [11,12].

In this work, HWCVD is employed to grow boron-doped silicon films using an altered filament configuration (AFC) which possesses more densely populated filaments than the conventional configuration. This generates a higher deposition temperature that could provide an in-situ annealing effect during film growth. The deposition temperature is measured using this configuration and compared to the conventional filament configuration (NFC). P-N junctions are then fabricated using a refined fabrication recipe that includes a short post-deposition anneal. The crystallinity and morphological characteristics of the films are studied using transmission electron microscopy (TEM) for imaging and selective-area electron diffraction (SAED), Raman spectroscopy and X-ray diffraction (XRD). Furthermore, the doping profiles are measured and compared using secondary ion-mass spectrometry (SIMS) for determining the film dopant levels and dopant diffusion into the substrate. Finally, current-voltage (I-V) measurements on HWCVD-formed diodes are taken under dark conditions and analysed.

* Corresponding author.
*E-mail address:* ek9g13@soton.ac.uk (E. Khorani).

https://doi.org/10.1016/j.tsf.2020.137978
Received 20 September 2019; Received in revised form 4 March 2020; Accepted 23 March 2020
Available online 14 April 2020

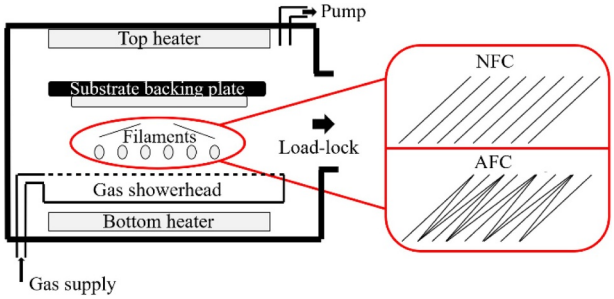


**Fig. 1.** Simplified schematic of HWCVD chamber with NFC and AFC illustrated.

## 2. Experimental details

### 2.1. HWCVD filament arrangement & deposition temperature monitoring system

Deposition temperature of the HWCVD tool (a Nitor 301 HWCVD system from ECHERKON Technologies Ltd.) was measured under two filament configurations. These filament arrangements are NFC, consisting of 0.18 mm tungsten filaments arranged in a parallel format with 2 cm spacing, and AFC, that consists of a more densely populated arrangement with crossing filaments in between the parallel filaments. The effect of two supplementary heaters set at 550 °C is also demonstrated as their influence on the deposition temperature was measured under the two filament configurations of interest. A simplified illustration of the HWCVD chamber is presented in Fig. 1. The substrate is placed on a backing plate, 5 cm above the filaments. The two filament configurations of interest, namely NFC and AFC, are also illustrated in a simplified format in Fig. 1.

The electrical power supplied to the filaments is configured based on the filament thickness, filament arrangement and filament temperature. The filament conditions of the HWCVD chamber during these measurements under NFC and AFC are shown in Table 1.

A higher potential difference is required for the larger density of filaments in place, meaning an increase of power usage under the AFC arrangement. The maximum filament temperature we can apply is 2100 °C based on the current limit of 120 A and to avoid Tungsten evaporation. This is compared to 1850 °C which is the filament temperature typically used for amorphous silicon depositions. The effect of using the top and bottom heaters set at 550 °C is also measured.

To accurately measure the deposition temperature, a custom-built temperature measurement system was devised. This consists of a Type K thermocouple ceramically adhered (using AREMCO adhesives) to the centre of a 4″ float-zone (FZ), 280 μm thick silicon wafer. This wafer was placed in the chamber with the cold junction of the thermocouple being fed out of the chamber and connected to an analog Devices AD8495 chip. The signal is filtered and amplified before being fed to a voltmeter where the potential difference is converted to a temperature difference based on the Seebeck effect.

### 2.2. Sample preparation

Boron-doped silicon films were deposited on 4″ n-type wafers (FZ, 1–5 Ω-cm, ⟨100⟩, 280 μm) with a pre-deposition immersion in 7:1 hydrofluoric acid for 30 s for native oxide removal. All depositions are conducted at a chamber pressure of 1.3 Pa. The growth recipe via HWCVD includes an intrinsic buffer layer deposited using silane ($SiH_4$) at 3 sccm for 4 min. Boron-doped silicon is then grown using $SiH_4$ and diborane ($B_2H_6$) at a 10/10 sccm gas flow ratio for 23 min. Following the filament configuration study, all subsequent films were deposited with the AFC configuration.

To study the effects of heat treatment on the structural and electrical characteristics of these silicon films, a post-deposition anneal at 800 °C for 2 min in $N_2$ atmosphere using a JipElec rapid thermal anneal chamber was conducted. The temperature and duration for this anneal step was optimised in previous studies [13]. Raman spectroscopy of samples with higher temperature anneals was employed to study Fano resonances from the dopant diffusion in the annealed films.

For dark I-V measurements, 1 μm of Al was deposited on both sides of the wafer via thermal evaporation using a Leybold BAK600 e-beam evaporator to form contacts to both sides of the p-n junction.

**Table 1**
Filament conditions for NFC and AFC arrangement.

| Configuration | Filament temp.( °C) | Voltage (V) | Current (A) |
|---|---|---|---|
| NFC | 1850 | 25.0 | 90.0 |
| | 2100 | 33.0 | 115.1 |
| AFC | 1850 | 30.0 | 98.1 |
| | 2100 | 38.0 | 114.5 |

### 2.3. Characterisation

TEM imaging of the boron-doped silicon films is carried out using a JEOL JEM-F200 electron microscope, providing a point resolution of 0.19 nm. This was operated at an accelerating voltage of 200 kV. Selective area electron diffraction was conducted at a 400 mm camera length using a GATAN OneView camera. The TEM samples were prepared using a FEI Quanta 200 3D FIB.

Raman spectroscopy is used to characterise the crystallinity of the silicon films, both before and after annealing. This is done using a Renishaw inVia confocal Raman microscope with a 532 nm laser at 5% laser power and 3 s laser exposure. X-ray diffraction spectroscopy is done using a Rigaku SmartLab diffractometer and a 9 kW (45 kV, 200 mA) Cu target rotating anode generator and a HyPix 3000 semiconductor detector. This was conducted using grazing incidence at a low X-ray grazing angle of 1°.

Secondary ion mass spectrometry is conducted using an ION TOF ToF-SIMS 5 instrument with silicon and boron ions detected during milling. A relative sensitivity factor (RSF) was applied to the raw-counts data to convert to boron concentration, with the RSF being measured and calibrated for boron in silicon. I-V measurements are taken under dark conditions using a Keithley set-up and LabVIEW interface.

## 3. Results and discussion

### 3.1. HWCVD deposition temperature measurements

The deposition temperature results are presented in Fig. 2. The AFC is shown to give a higher deposition temperature in all cases, increasing by 7–13% from the NFC. For epitaxial growth, we are interested in the higher limits of the deposition temperatures available. Using both heaters and filaments at 2100 °C, an increase from 498 °C to 535 °C is achieved from the NFC to AFC, respectively. This boost in temperature is promising towards enhancing the in-situ annealing effect during the silicon film growth, as this ought to produce larger grains and higher uniformity. However, even with the AFC, the deposition temperature is insufficient to achieve epitaxial growth as we would expect this with a deposition temperature exceeding 610 °C based on previous reports from the literature [2,10].

### 3.2. Film morphology

#### 3.2.1. Transmission electron microscopy imaging

TEM can provide real-space information on the atomic plane orientation and crystallographic structure of films of interest via high-resolution imaging. Fig. 3(a) and 3(b) illustrate the as-deposited and annealed boron-doped silicon films, respectively. The interface and crystalline substrate are identified in these images, allowing us to analyse the crystallinity of the deposited layer in comparison to the

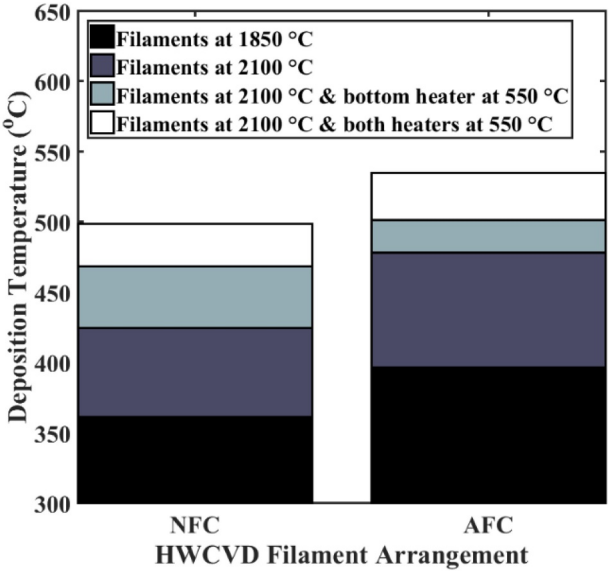


**Fig. 2.** Deposition (substrate) temperature measurements of HWCVD taken under NFC and AFC.

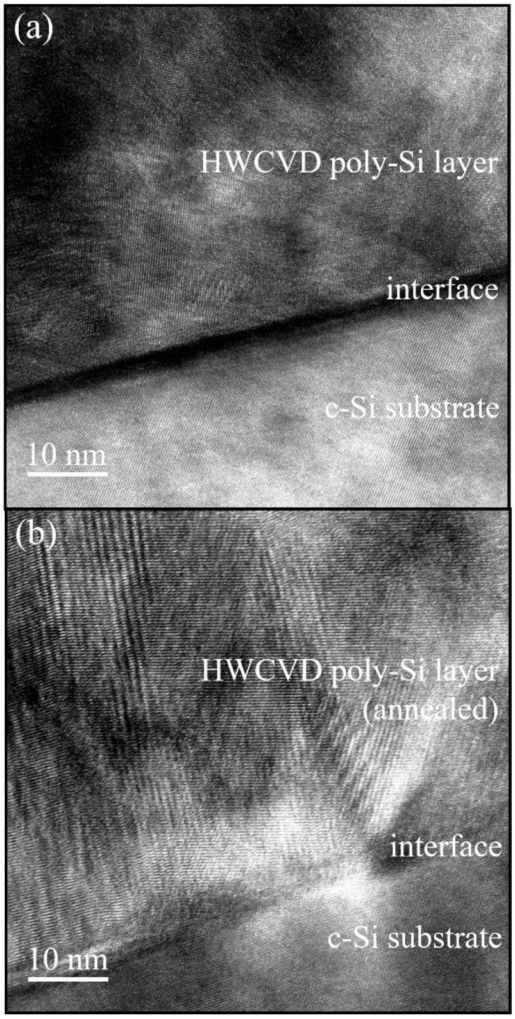


**Fig. 3.** TEM images of (a) as-deposited silicon and (b) annealed silicon films grown via AFC−HWCVD.

single crystal substrate as well as study the interfacial quality.

The thickness of the deposited film is measured as 220 nm via TEM imaging, suggesting a deposition rate of 0.17 nm/s. This a relatively slow when compared to deposition rates of up to 110 nm/min in literature [14], but it allows for a more controlled growth process which avoids the formation of pinholes or blisters. The grains present on both films show crystalline properties, with uniformity in atomic plane orientation in certain regions. The heterogeneity of the grains suggests polycrystalline properties. Smaller grains can be observed in Fig. 3(a) in the deposited silicon film in comparison to the relatively larger grains visible in Fig. 3(b) in the annealed case, illustrating that the annealing step has crystallised the film further.

The interface between the deposited silicon and bulk substrate in the as-deposited case is shown in Fig. 3(a). This illustrates void-like features with minimal evidence of lattice matching between the bulk and the deposited silicon. On the other hand, the interface of the annealed sample in Fig. 3(b) appears significantly more uniform, with matching regions between the atomic plane orientation of the silicon atoms from the bulk (<100>) directly to the polycrystalline silicon layer. The heterogeneities in the interface could introduce defects that would be detrimental to the transport of charge carriers through the p-n junction. The reduction in voids and enhancement in lattice matching suggests an enhancement in interfacial quality from the short post-deposition anneal. This would translate as an improvement in the overall carrier transport efficiency when used as an emitter in a solar cell [2,9,10].

### 3.2.2. *Selective-area electron diffraction*

SAED is used for examining the crystal structure in different regions of the p-n junction. Using this technique, the resulting diffraction patterns are either spot patterns that correspond to single-crystal diffraction or ring patterns corresponding to diffraction from multiple crystals [15]. In cases where amorphous silicon is present, the ring patterns overlap to form an annulus.

The diffraction patterns taken from different regions of the as-deposited sample and the annealed sample are shown in Fig. 4(a) − 4(c) and Fig. 4(d) − 4(f) respectively. The bulk substrate of both samples in Fig. 4(a) and Fig. 4(d) appears as spot patterns, suggesting monocrystalline properties, as expected from the FZ wafers used in this work. The diffraction pattern of the interface region in both cases in Fig. 4(b) and Fig. 4(e) show concentric rings as well as spot patterns, indicating the transition from monocrystalline to polycrystalline from substrate into the film. Nonetheless, it is evident that the ring patterns are visibly less dominant in the interface of the annealed case in comparison to the as-deposited interface region. This supports the enhancement in lattice alignment seen in the interface region of the annealed sample in Fig. 3(b), as a stronger dominance from the ⟨100⟩ plane in this region

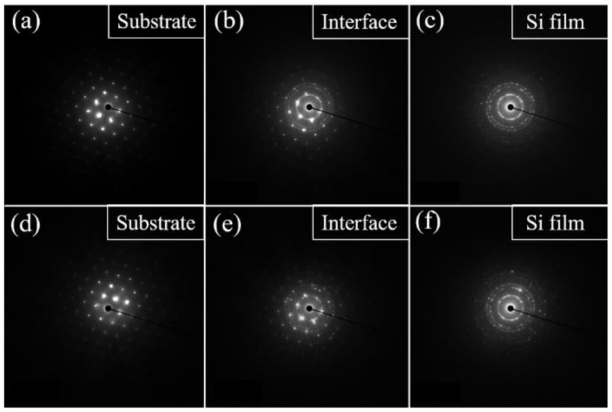


**Fig. 4.** Selective-area electron diffraction patterns taken from (a)-(c) deposited silicon and (d)-(f) annealed silicon films grown via AFC−HWCVD.

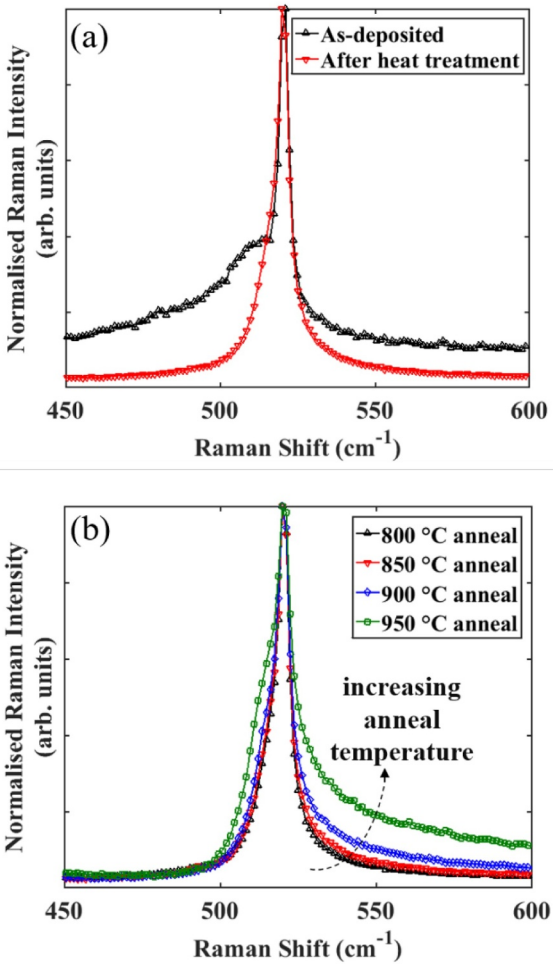


**Fig. 5.** Raman spectra of (a) deposited and annealed film, and (b) films annealed at temperatures between 800 °C – 950 °C.

translates as clearer spots rather than ring patterns. Fig. 4(c) and Fig. 4(f) show the diffraction pattern taken from the deposited silicon layer of the as-deposited and annealed structures respectively. The clear ring patterns are supportive of this film being polycrystalline in both cases. The lack of a clear spot pattern suggests there is no dominant plane orientation present in this film.

### 3.3. Film crystallinity

#### 3.3.1. Raman spectroscopy

Raman spectroscopy can be employed to investigate the structural changes in silicon [16]. The Stokes Raman spectra of the as-deposited and annealed silicon layer are displayed in Fig. 5(a). The spectral region of interest is 480 – 520 $cm^{-1}$. A crystalline silicon peak is expected at 520 $cm^{-1}$. The presence of polycrystalline material results in the peak shifting left as crystalline size decreases, reaching 512 $cm^{-1}$ for microcrystalline silicon and 510 $cm^{-1}$ for nanocrystalline silicon. Amorphous silicon gives a peak at 480 $cm^{-1}$ [17,18]. The peak at 520 $cm^{-1}$ is from the substrate. For the as-deposited silicon, we see a broad shoulder-like peak present that extends from 512 $cm^{-1}$ up to 480 $cm^{-1}$ in wavenumber. When defined as a Voigt profile, this peak can be identified as the convolution of two peaks that represent both microcrystalline and amorphous characteristics of this film. This suggests that this film is deposited as polycrystalline, being composed of amorphous, crystalline and intermediate regions. When annealed for 2 min at 800 °C, the shoulder disappears and now only a peak at 514 $cm^{-1}$ is

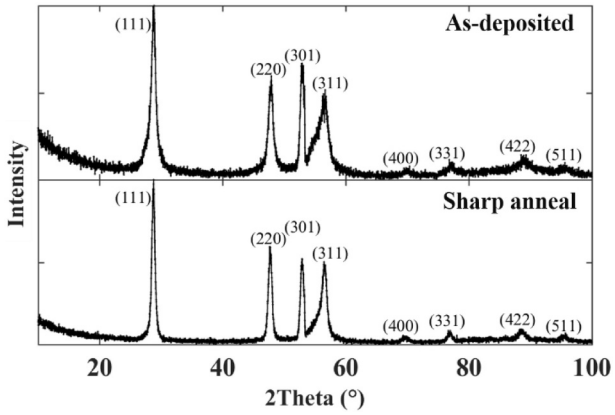


**Fig. 6.** X-ray diffraction pattern of as-deposited and annealed HWCVD films.

convolved with the 520 $cm^{-1}$ peak from the bulk. This shows that the short heat treatment step has crystallised any remnant amorphous silicon and an increase in crystal size is evident based on the shift in the microcrystalline peak from 512 $cm^{-1}$ to 514 $cm^{-1}$.

Fig 5(b) shows the effect of the temperature of the short anneal step via rapid thermal annealing. Whilstno significant alteration in crystallinity was observed, a tailing off effect on the right side of the Raman peak was seen with the peak developing increasing asymmetry with higher anneal temperatures. This tail, seen either on the left side (n-type doping) or right side (p-type doping) of the Raman peak, is known as Fano-type resonance [17,19]. This can typically occur when there is dopant diffusion into the bulk, causing a resonant interaction between the discrete optical phonon states and the continuum of energy levels in the valence and conduction bands. This interaction between the Raman scattering and electron Raman scattering is due to electron-phonon coupling and thus induces a Fano-type silicon Raman peak asymmetry.

#### 3.3.2. X-ray diffraction

The XRD patterns for the deposited and heat-treated films are shown in Fig. 6. The peaks associated to the different crystal orientations of silicon are identified. Both films display a similar peak pattern representing polycrystalline properties [20,21]. A single peak at 69 ° (<400>) would be expected if the film was monocrystalline (i.e. silicon epitaxy). The dominance of the ⟨111⟩ peak is evident for both films and is indicative of the presence of polycrystalline silicon.

Based on our morphological characterisation, it is evident that we can grow polycrystalline silicon via the AFC—HWCVD growth process with enhancement in crystalline structure and interfacial properties achieved using a short post-deposition heat treatment. The crystallinity of the as-deposited film is also enhanced by crystallising any amorphous silicon present via annealing. Whilst there is no epitaxial growth, as expected from the deposition temperature measurements, some lattice matching in the interface region is evident post-annealing.

### 3.4. Electrical characteristics

#### 3.4.1. Boron doping via secondary ion-mass spectrometry

SIMS is used to measure the boron doping profile of the HWCVD polycrystalline silicon films. Fig. 7 shows the doping profile of the deposited and heat-treated films as a function of depth. Both films show a degree of uniformity in doping within their bulk, to the order of $10^{21}$ $cm^{-3}$ boron concentration. A rapid decay of dopant concentration towards the interface region is observed for the annealed case. This is due to the dopants being driven through the interface and into the bulk, as observed from the presence of boron dopants up to 600 nm beyond the junction (as shown in the inset in Fig. 7) for the heat-treated sample. This is not the case with the as-deposited sample as the concentration of boron dopants remains high up to the interface in the SIMS profile and

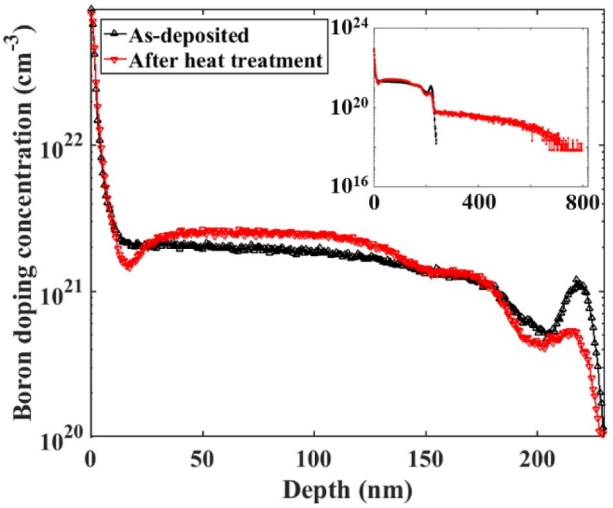


**Fig. 7.** Boron doping as a function of depth for as-deposited and annealed films taken from secondary ion-mass spectrometry.

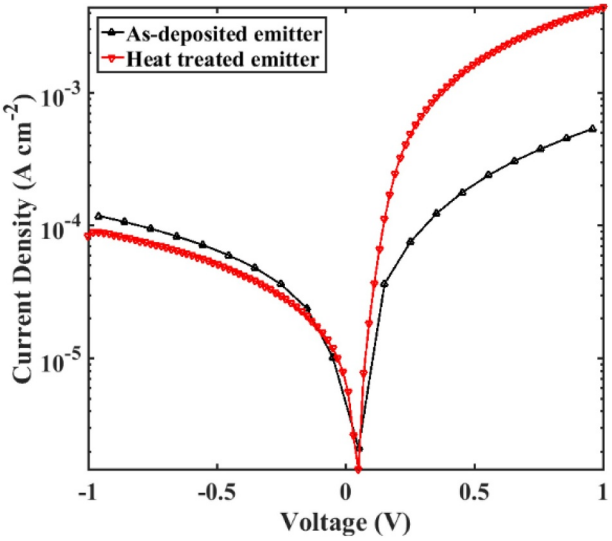


**Fig. 8.** Dark current-voltage results for as-deposited and annealed emitter films grown via HWCVD.

decays very abruptly. The high level of doping ($>10^{18}$ cm$^{-3}$) and the diffusion of dopants through the interface into the bulk region supports the Fano-type resonant interaction observed in the Raman results presented in Fig. 5(b). The high doping concentration is useful for increasing conductance in this region that in turn can be utilized for polysilicon passivating contacts in silicon solar cells, where high conductivity and a low minority carrier recombination velocity are of primary interest. There is however a trade-off with the increased Auger recombination due to higher doping.

The kink observed in the 205–210 nm region for both films can be due to the adsorption of dopants to the walls of the HWCVD chamber during the initial growth period. Once the chamber is saturated, the doping concentration stabilises. One potential way of eliminating this effect could be to saturate the chamber with $B_2H_6$ prior to $SiH_4$ flow. In addition, a sharp increase in boron dopants (exceeding $10^{22}$ cm$^{-1}$) can be observed in the top 10 nm of the film. Likewise, a rapid decrease in the raw counts data for silicon is observed at the same top region of the film (see supplementary data). This occurs at the latter stages of the deposition process when the $SiH_4$ and $B_2H_6$ flow has been terminated, but deposition continues for a short period as boron dopant atoms desorb from the chamber walls.

### 3.4.2. Dark current-voltage extraction

I-V measurements under dark conditions are taken to measure the effect of the sharp annealing step on the electrical characteristics of this film as an emitter. Fig. 8 shows the current density as a function of the voltage swept between −1 V and +1 V, demonstrating the annealing effects.

The ratio of the current density taken at +1 V and −1 V is known as the rectification factor and can be used as a figure of merit to compare diode performance. A boost from 5 to 55 in the rectification factor is observed by annealing the film for 2 min at 800 °C. This agrees with the morphological improvements seen in previous sections of this work. This improvement could be explained by the improvement in interfacial quality seen in the TEM images in Fig. 2, as this would translate as an enhancement in carrier mobility in this region and hence current extraction. The crystallisation of remnant amorphous silicon in our films, the larger grains and higher uniformity from annealing could also be contributing to this improvement. Furthermore, dopant diffusion beyond the interface could also lead to higher current density (at 1 V) by improving the conductivity of this area.

To analyse the effect of annealing on the diode characteristics further, the I-V characteristics from Fig. 8 are fitted to a two-diode model. The model used is derived in literature [22] following the equation:

$$J = J_{01}e^{\frac{q(V-JR_s)}{n_1kT}} + J_{02}e^{\frac{q(V-JR_s)}{n_2kT}} + \frac{V-JR_s}{R_{sh}}$$

Where $R_s$ and $R_{sh}$ are the series and shunt resistances, $J_{01}$ and $J_{02}$ are the dark saturation currents and $n_1$ and $n_2$ are the ideality factors for the ideal and non-ideal diodes in the equivalent circuit of the two-diode model, respectively. The I-V data is fitted to this model using an online open-source tool (2/3 Diode Fit) [23]. The results are shown in Table 2.

A reduction in both saturation currents is seen post-annealing. Furthermore, a higher shunt resistance and lower series resistance is derived for the annealed diode. A small reduction in the ideality factor for the ideal diode ($n_1$) is also observed. The reduction in saturation current can support the improvement in junction quality as this would suggest a reduction in carrier recombination losses at the interface, further supported by the increase in shunt resistance. These changes support the improvement in diode characteristics after annealing, indicating a higher carrier collection efficiency and lower shunting losses in our diode. Despite these improvements, the absolute values for saturation currents are considerably high due to the lack of passivating material for non-contacted regions and no optimization of the ohmic contacts.

## 4. Conclusion

A HWCVD deposition temperature boost from 498 °C to 535 °C using a more densely populated filament arrangement was recorded. The polycrystalline nature of the as-grown boron-doped films is evident from TEM images and further confirmed by Raman spectroscopy and XRD. With a sharp post-deposition anneal, an enhancement is seen resulting in larger crystals and a less-defective interface. Furthermore, remaining traces of amorphous silicon are crystallised by the short anneal. The results confirm $p^+$ properties with stable doping in the $10^{21}$ cm$^{-3}$ region as well as the presence of dopant diffusion beyond the grown interface up to 600 nm in the bulk after the anneal step.

**Table 2**
Two-diode model parameters extracted for as-deposited and annealed AFC–HWCVD films.

| HWCVD film | $J_{01}$ (nA/cm$^2$) | $J_{02}$ (nA/cm$^2$) | $R_s$ (Ω/cm$^2$) | $R_{sh}$ (Ω/cm$^2$) | $n_1$ | $n_2$ |
|---|---|---|---|---|---|---|
| As-deposited | 5.2 | 405 | 1520 | 6730 | 2.2 | 1 |
| Annealed | 2.9 | 57 | 735 | 46,040 | 2.0 | 1 |

Finally, dark current-voltage measurements show that a boost in current rectification factor is achieved by annealing the HWCVD grown films, with improvements in diode characteristics suggested by fitting to a two-diode model. Future work towards making these emitters fit for use in solar cells will focus on reducing carrier recombination by employing ultrathin passivating layers at the interface between the film and substrate.

## Declaration of Competing Interests

None.

## Acknowledgments

This work was supported by the Centre for Doctoral Training in New and Sustainable Photovoltaics (EP/L01551X/1); the Supergen Solar Network + (EP/S000763/1); and Black Silicon Photovoltaics (EP/R005303/1). This work was also supported by the Henry Royce Institute for Advanced Materials, funded through EPSRC grants EP/R00661X/1, EP/P02470X/1, EP/P25285/1 and EP/S019367/1.

## References

[1] International technology roadmap for photovoltaics, ITRPV roadmap 2019. https://itrpv.vdma.org/en/, 2019 (accessed 18 July 2019).
[2] A. Ingenito, O. Isabella, M. Zeman, Simplified process for high efficiency, self-aligned IBC c-Si solar cells combining ion implantation and epitaxial growth: design and fabrication, Sol. Energy Mater. Sol. 157 (2016) 354–365, https://doi.org/10.1016/j.solmat.2016.05.021.
[3] E. Franklin, K. Fong, K. McIntosh, A. Fell, A. Blakers, T. Kho, D. Walter, D. Wang, N. Zin, M. Stocks, E. wang, N.E. Grant, Y. Yang, X. Zhang, Z. Feng, P.J. Verlinden, Design, fabrication and characterisation of a 24.4% efficient interdigitated back contact solar cell, Progress Photovoltaics: Res. Appl. 15 (2014) 659–676, https://doi.org/10.1002/pip.2556.
[4] National Renewable Energy Laboratory, Best research-cell efficiencies chart. https://www.nrel.gov/pv/cell-efficiency.html, 2019(accessed 18 July 2019).
[5] T. Rahman, A. To, M.E. Pollard, N.E. Grant, J. Colwell, D.N.R. Payne, J.D. Murphy, D.M. Bagnall, B. Hoex, S.A. Boden, Minimising bulk lifetime degradation during the processing of interdigitated back contact silicon solar cells, Progress Photovoltaics: Res. Appl. 26 (1) (2017) 38–47, https://doi.org/10.1002/pip.2928.
[6] M. Justianto, T. Harig, M. Höfer, V. Sittinger, Silicon films for heterojunction solar cells by hot-wire cvd, AIP Conf. Proc. 2147 (2019) 050006, , https://doi.org/10.1063/1.5123855.
[7] R.E.I. Schropp, Industrialization of hot wire chemical vapor deposition for thin film applications, Thin Solid Films 595 (2015) 272–283, https://doi.org/10.1016/j.tsf.2015.07.054.
[8] S. Wagner, D.E. Carlson, H.M. Branz, Amorphous and microcrystalline silicon solar cells, NREL/CP-520-29586, 1999, 13 pp. https://pdfs.semanticscholar.org/92c2/5db38ebea6737e2422adb5978fdeaa9d693c.pdf.
[9] T. Rahman, H.T. Nguyen, A. Tarazona, J. Shi, Y. Han, E. Franklin, D. Macdonald, S.A. Boden, Characterization of epitaxial heavily doped silicon regions formed by hot-wire chemical vapor deposition using micro-raman and micro-photoluminescence spectroscopy, IEEE J. PV 8.3 (2018) 813–819, https://doi.org/10.1109/JPHOTOV.2018.2818284.
[10] M.R. Payo, N. Posthuma, A. Uruena de Castro, M. Debucquoy, J. Poortmans, Boron-doped selective silicon epitaxy: high efficiency and process simplification in interdigitated back contact cells, Progress Photovoltaics: Res. Appl. 15 (2013) 711–725, https://doi.org/10.1002/pip.2427.
[11] H. Matsumura, K. Higashimine, K. Koyama, K. Ohdaira, Comparison of crystalline-silicon/amorphous-silicon interface prepared by plasma enhanced chemical vapor deposition and catalytic chemical vapor deposition, J. Vac. Technol. 33 (2015) 031201, , https://doi.org/10.1116/1.4915494.
[12] T. Rahman, A. Nawabjan, A. Tarazona, D.M. Bagnall, S.A. Boden, Junction formation with HWCVD and TCAD model of an epitaxial back-contact solar cell, IEEE J. PV 6.6 (2016) 1396–1402, https://doi.org/10.1109/JPHOTOV.2016.2598277.
[13] E. Khorani, T.E. Scheul, A. Tarazona, T. Rahman, S.A. Boden, Optimisation of Ex-Situ Annealing Process For Epitaxial Silicon Emitters Via Hot Wire CVD, PV-SAT 14, Warwick, UK, April 2018https://www.pvsat.org.uk/repository/archive.htm.
[14] Q. Wang, C.W. Teplin, P. Stradins, B. To, K.M. Jones, H.M. Branz, Significant improvement in silicon chemical vapor deposition epitaxy above the surface dehydrogenation temperature, J. App. Phys. 93520 (2006) 9–14, https://doi.org/10.1063/1.2363766.
[15] J.M. Cowley, Crystal structure determination by electron diffraction, Prog. Mat. Sci. 13 (1968) 267–321, https://doi.org/10.1016/0079-6425(68)90023-6.
[16] C. Wen, Y.J. Yang, Y.J. Ma, Z.Q. Shi, Z.J. Wang, J. Mo, T.C. Li, X.H. Li, S.F. Hu, W.B. Yang, Sulfur-hyperdoped silicon nanocrystalline layer prepared on polycrystalline silicon solar cell substrate by thin film deposition and nanosecond-pulsed laser irradiation, Appl. Surf. Sci. 476 (2019) 49–60, https://doi.org/10.1016/j.apsusc.2019.01.074.
[17] G. Sarau, A. Bochmann, R. Lewandowska, S. Christiansen, From micro to macro raman spectroscopy: solar silicon for a case study, in: M.A. Farrukh (Ed.), Advanced Aspects of Spectroscopy, IntechOpen, 2012, pp. 221–246 https://www.intechopen.com/books/advanced-aspects-of-spectroscopy/from-micro-to-macro-raman-spectroscopy-solar-silicon-for-a-case-study.
[18] T. Kaneko, K. Onisawa, M. Wakagi, Y. Kita, T. Minemura, Crystalline fraction of microcrystalline silicon films prepared by Plasma- Enhanced Chemical vapour deposition using pulsed silane flow, Jpn. J. Appl. Phys. 32 (1993) 4907–4911, https://doi.org/10.1143/JJAP.32.4907.
[19] M. Becker, U. Gosele, A. Hofmann, S. Christiansen, Highly p–doped regions in silicon solar cells quantitatively analysed by small angle bevelling and micro-Raman spectroscopy, J. Appl. Phys. 106 (2009) 074515, , https://doi.org/10.1063/1.3236571.
[20] J.S. Kasper, S.M. Richards, The crystal structure of new forms of silicon and germanium.", Acta Crystallogr. 17 (1964) 752–755, https://doi.org/10.1107/S0365110X64001840.
[21] R.T. Downs, K.L. Bartelmehs, G.V. Gibbs, M.B. Boisen, Interactive software for calculating and displaying X-ray or neutron powder diffractometer patterns of crystalline materials, Am. Mineralogist 78 (1993) 1104–1107 https://arizona.pure.elsevier.com/en/publications/interactive-software-for-calculating-and-displaying-x-ray-or-neut.
[22] M. Wolf, H. Rauschenbach, Series resistance effects on solar cell measurements, Adv. Energy Convers. (1963) 455–479, https://doi.org/10.1016/0365-1789(63)90063-8 3.2.
[23] S. Suckow, 2/3-Diode Fit, http://nanohub.org/resources/14300/, 2014(accessed 1 May 2019).